Ultrafast Control of Excitonic Rashba Fine Structure by Phonon Coherence in the Metal Halide Perovskite CH₃NH₃PbI₃

Z. Liu,[1,†] C. Vaswani,[1,†] X. Yang,[1] X. Zhao,[1] Y. Yao,[1] Z. Song [ORCID],[2] D. Cheng,[1] Y. Shi [ORCID],[3] L. Luo,[1] D.-H. Mudiyanselage,[1] C. Huang [ORCID],[1] J.-M. Park,[1] R. H. J. Kim [ORCID],[1] J. Zhao,[3] Y. Yan,[2] K.-M. Ho,[1] and J. Wang [ORCID][1,*]

[1]*Department of Physics and Astronomy and Ames Laboratory-U.S. DOE, Iowa State University, Ames, Iowa 50011, USA*
[2]*Department of Physics and Astronomy and Wright Center for Photovoltaics Innovation and Commercialization,*
The University of Toledo, Toledo, Ohio 43606, USA
[3]*ICQD/Hefei National Laboratory for Physical Sciences at the Microscale,*
and Key Laboratory of Strongly-Coupled Quantum Matter Physics,
Chinese Academy of Sciences, University of Science and Technology of China,
Hefei, Anhui 230026, China

We discover hidden Rashba fine structure in CH₃NH₃PbI₃ and demonstrate its quantum control by vibrational coherence through symmetry-selective vibronic (electron-phonon) coupling. Above a critical threshold of a single-cycle terahertz pump field, a Raman phonon mode distinctly modulates the middle excitonic states with *persistent* coherence for more than ten times longer than the ones on two sides that predominately couple to infrared phonons. These vibronic quantum beats, together with first-principles modeling of phonon periodically modulated Rashba parameters, identify a threefold excitonic fine structure splitting, i.e., optically forbidden, degenerate dark states in between two bright ones with a narrow, ~3 nm splitting. Harnessing of vibronic quantum coherence and symmetry inspires light-perovskite quantum control and sub-THz-cycle "Rashba engineering" of spin-split bands for ultimate multifunction device.

DOI: 10.1103/PhysRevLett.124.157401

Fundamental understanding and light quantum control of metal halide perovskites are key to discovering new photovoltaic materials and multifunction spin-charge-photon devices. Methylammonium lead iodide, MAPbI₃, is illustrated in Fig. 1(a). Rashba-type effects, which control the direct or indirect nature of spin-split bands and fine structure splitting (FSS) [1,2], have been proposed to determine the outstanding, yet mysterious properties in perovskites [3]. These include, e.g., long photocarrier lifetimes [4], spin or charge diffusion lengths [5,6] and nonlinear optics [7]. The challenge to unambiguously detect the FSS in them lies in the vibronic fluctuations on short time and length scales associated with dynamical entropy and local symmetry breaking that seriously broaden band edge absorption discussed below. As illustrated in the Fig. 1(b) (inset) [8], the Rashba effects lift spin and momentum degeneracies in MAPbI₃ which leads to the excitonic FSS, where the four fold degeneracy of the 1s exciton is split by the Rashba terms $\alpha_{e(h)} \vec{\sigma}_{e(h)} \cdot \hat{n} \times i \vec{\nabla}_{r_{e(h)}}$. Here $\alpha_e(\alpha_h)$ and $\sigma_e(\sigma_h)$ denote the Rashba parameter and Pauli matrices for the $\mathbf{J} = 1/2$ ($\mathbf{S} = 1/2$) conduction (valance) band. Energy levels of the lowest-lying excitonic fine structure can be calculated based on these parameters [8] (see the Supplemental Material [9]) as two bright exciton states (green lines), $|\Phi_{1,4}\rangle$, lying above and below two degenerate dark states (blue lines), $|\Phi_{2,3}\rangle$, in MAPbI₃ [inset, Fig. 1(b)]. Consequently the bright and dark exciton splitting is only a few nm, ~10 times smaller than the
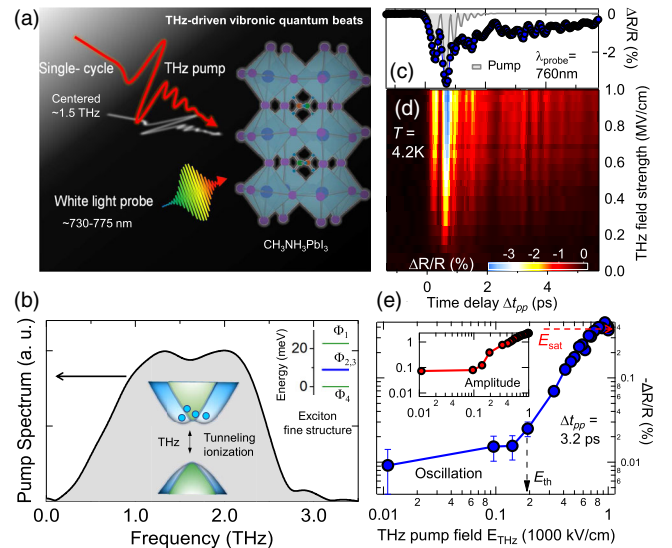

FIG. 1. (a) Schematics for THz pump and white light continuum probe spectroscopy in MAPbI₃. (b) THz pump spectrum (gray shade) shown together with an illustration of Rashba-type bands. (c) Representative $\Delta R/R$ dynamics at 760 nm probe induced by $E_{THz} = 938$ kV/cm at 4.2 K and (d) complete 2D false-color plot. Squared THz pump field is plotted together in (c) (gray shade). (e) Pump electric field dependence of amplitudes of the oscillatory (blue circles) and exponential decay (inset, red circles) components. See the Supplemental Material [9] for a detailed analysis (Fig. S3).

inhomogeneously broadened photoluminescence (PL) line-width (> 30 nm) [15,16], Supplementary Fig. 2. The presence of the FSS and dark states, the hallmark for the Rashba effects in perovskites, remain elusive until this work despite intense studies [8,15,17–22].

Coherent quantum beat spectroscopy driven by an intense single-cycle terahertz (THz) pulse, Fig. 1(a), is extremely relevant for discovery and control of the excitonic FSS. First, the deep sub-band-gap pump spectrum centered at ∼6.2 meV or 1.5 THz [gray, Fig. 1(b)] can lead to coherent excitation of phonons [23] with minimum heating. Such low energy, nonthermal pumping allows for the determination of the genuine ground state, with only few nm splitting, complementary to, e.g., high energy, optical pumping [24–26]. Second, in addition to the conventional THz phonon generation mechanism from photonic or ionic coupling [23], polaronic e-phonon coupling in perovskites allows for the generation of vibronic quantum beats from the intense THz pulse-driven tunneling ionization. Microscopically, this creates transient exciton population mediated by interband exciton coherence which, in turn, impulsively distorts vibrational potential and generates exciton band oscillations dressed by coherent phonons. Third, the driven "ultrafast-ultrasmall" lattice displacement senses the local dynamic dielectric environment and modulates excitons that can be probed by quantum beats. The dark states can be periodically brightened by broken symmetry coherent phonons, unlike thermal ones averaging to zero. This may determine the FSS by their *symmetry-selective* coupling to infrared (IR) or Raman modes that strongly modulate the spin-split bands. Such unique coherent phenomenon has never been observed.

Here we report vibronic quantum beats from the Rashba-type fine structure induced by an intense single-cycle THz field in bulk MAPbI$_3$ single crystals. This manifests as *symmetry-selective coupling* of dark and bright excitons to predominantly Raman and IR phonon coherence. The experiment was performed at 4.2 K in a single crystal MAPbI$_3$ sample in its orthorhombic phase. We performed single cycle intense THz pump and white light continuum probe spectroscopy with simultaneous fs temporal and sub-nm spectral resolutions (see the Supplemental Material [9]). Figure 1(c) shows a pronounced oscillatory behavior with complex beating patterns superimposed on a slow amplitude decay in the pump-induced differential reflectivity $\Delta R/R$ dynamics at 760 nm probe wavelength, i.e., the exciton peak at 4.2 K, after the sub-ps pump (gray shade) at $E_{THz} = 938$ kV/cm. A complete 2D false-color plot of $\Delta R/R(\Delta t_{pp}, E_{THz})$ is shown in Fig. 1(d) as a function of time delay Δt_{pp} up to 5.7 ps and E_{THz} pump up to ∼1000 kV/cm. This allows to extract the amplitudes associated with the oscillatory [Fig. 1(e)], and exponential decay components (inset). Intriguingly, the THz field dependence shows a clear nonlinearity with a thresholdlike turning on of a new quantum process, i.e., the critical feature for the tunneling ionization with a threshold

$E_{th} \sim 200$ kV/cm in the beating signals. A saturation of excitonic signals is seen at $E_{sat} \sim 1000$ kV/cm. Note that the vibronic quantum beats here exhibit much more complex patterns than previously observed in perovskites, e.g., up to 100 kV/cm [27]. One order of magnitude higher THz field strength used [28–32] and long-lived charge carrier dynamics after the pulse, from the transient population decay, clearly identify the roles of THz-driven tunneling ionization.

Figure 2 presents the spectral-temporal behavior of THz pump-induced $\Delta R/R$. The broadband probe light ranging from 730 to 773 nm is spectrally resolved after the sample and used to probe excitonic states in MAPbI$_3$ after THz excitation $E_{THz} = 938$ kV/cm. The transient spectra exhibit a broad bipolar, inductive line shape [Fig. 2(a)] of ∼30 nm width, i.e., a positive $\Delta R/R$ change switches to negative at 755 nm. Most intriguingly, the positive (∼751 nm), negative peaks (∼757 nm), and zero crossing (∼755 nm) (dashed lines) show negligible spectral shift during the large $\Delta R/R$ change, as shown at time delay $\Delta t_{pp} = 0.22$ ps (red diamond) and 3.7 ps (blue circle). The much narrower ∼3 nm separation marked in Fig. 2(a) is much smaller than the PL linewidth (∼30 nm, Fig. S2, [9]) and spectral shift (> 100 nm) in the prior excited state studies by optical pumping [17,25]. The latter can be explained largely by the exciton peak shift and broadening nonlinearities induced by the presence of photoexcited hot carriers. In contrast, the low-frequency, THz pumping data indicates a *stable*, narrow threefold structure, only seen by such nonthermal pumping, which is generic and determined mostly by ground state excitonic structure.

Next we present wavelength-dependent quantum beat spectra and dynamics that support the hidden threefold FSS
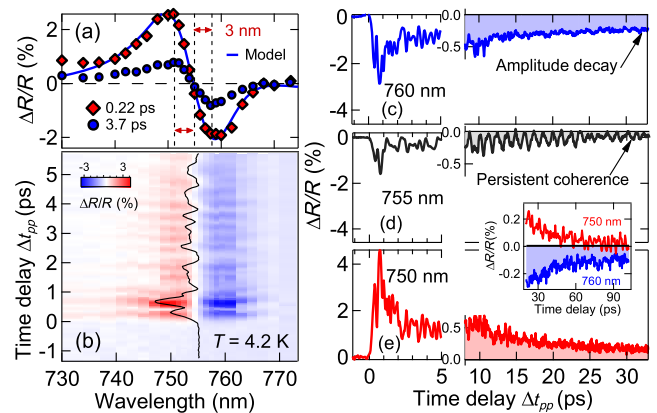

FIG. 2. (a) A time cut, $\Delta R/R$ spectrum at $\Delta t_{pp} = 0.22$ ps (red) and 3.7 ps (blue) from 2D false-color plot of THz pump-induced white light spectra in (b). Three stable spectral positions marked, i.e., positive (negative) peaks and zero crossing. Shown together in (a) is an oscillator model simulation [blue line, see Eq. (2) for details]. (c)–(e): The wavelength cut, three $\Delta R/R$ dynamics are shown at 760 nm (blue), 755 nm (black), and 750 nm (red), respectively. Inset of (d) and (e): clearly longer amplitude decay at the 760 nm trace than the 750 nm one up to 100 ps.

structure inside the inhomogeneously broadened exciton peak. First, there exhibit coherent oscillations with similar patterns on the two sides of the $\Delta R/R$ 2D plot in Fig. 2(b). Interestingly, very different oscillations are observed in the center within a very narrow linewidth ~ 3 nm near the zero crossing position of a broad, ~ 30 nm $\Delta R/R$ response; e.g., a representative time scan trace is shown near the transition point (black line). The different beat patterns from the center to the sides become even more clear by comparing three wavelength-cut dynamics, i.e., the middle, 755 nm probe trace near the zero-crossing position [black, Fig. 2(d)] exhibits remarkably long-lasting quantum oscillations shown for the first 5 ps and for the extended timescales up to many tens of ps (split axis), while the 760 nm [blue, Fig. 2(c)] and 750 nm [red, Fig. 2(e)] traces on the two sides near negative and positive peaks [Fig. 2(b)] have much shorter-lived quantum beats mostly within ~ 5 ps. This clearly shows that central exciton state is different from the two sides.

Second, although the two exciton sidebands at 760 and 750 nm show a quasisymmetric temporal beating pattern within ~ 5 ps, their long time $\Delta R/R$ (population) signals after dephasing show different relaxation times with clearly longer-lived signal (> 100 ps) at the lower, 760 nm trace than the 750 nm one [inset, Figs. 2(d) and 2(e)]. This clearly shows that two sidebands are also different from each other. The longer decay in the 760 nm trace is consistent with the fact that the final transient carrier recombination arises from the lowest bright exciton. Therefore, such asymmetry of the amplitude decay on two sides together with the "sharp" appearance of new oscillations [Fig. 2(d)] exclusively in the middle cannot be accounted by a single exciton oscillator. These distinguishing features are consistent with the periodically brightened, dark states in the center with persistent quantum coherence and a narrow linewidth since they are much less coupled to the dielectric environment. They are different from the bright states on two sides that are expected to exhibit shorter coherence (and much broader linewidth).
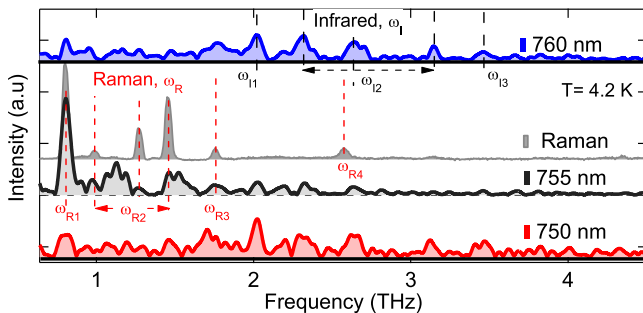

FIG. 3. Fourier spectra of three $\Delta R/R$ dynamics in Figs. 2(c)–2(e), shown together with the static Raman spectrum (gray shade) at 4.2 K. Note the pronounced Raman mode $\omega_{R1} \sim 0.8$ THz and IR phonon mode $\omega_{I1} \sim 2$ THz. The assignment and symmetry analysis of other Raman and IR modes are shown in Fig. S6 [9].

Figure 3 further reveals the distinct wavelength-dependent phonon modes which disclose a *symmetry-selective* coupling to the excitonic FSS in MAPbI$_3$. The Fourier transformation (FT) spectra of quantum beats are shown for the same three excitonic states at 760 nm (blue), 755 nm (black), and 750 nm (red) in Figs. 2(c)–2(e), respectively. The low-frequency Raman spectrum (gray shade) from the same conditions is shown together to identify the mode symmetry. The FT spectrum at the center band clearly displays a pronounced peak at $\omega_{R1} = 0.8$ THz that matches very well with the dominant transverse optical Raman mode from octahedral twist of PbI$_6$ cage [33]. Besides the main peak, there exist multiple secondary peaks mostly below 2 THz that correlate with the THz Raman modes $\omega_{R2}–\omega_{R4}$ (red lines) [9]. In strong contrast, the ω_R mode is strongly suppressed in the FT spectra of the side excitonic bands at 750 and 760 nm, which, instead, exhibit multiple strong peaks ≥ 2 THz, quasisymmetrically present (black dash lines), i.e., $\omega_{I1} = 2$ THz, $\omega_{I2} = 2.3$ THz, 2.66 THz, 3.1 THz, and $\omega_{I3} = 3.4$ THz [9]. They are absent in the measured THz Raman spectrum (gray shade) but mostly consistent with the reported IR phonon modes [33,34]. Prior Raman and linear THz spectra of MAPbI$_3$ reveal the phonon symmetry, IR and Raman activities, and electron-phonon coupling [33]. In the range of 1–4 THz relevant for our experiment, the phonon modes can be understood as a coupled motion of the octahedral cages and associated organic cations. Most intriguingly, the distinct comparisons for different probe wavelength in Fig. 3 indicate the preferred coupling of the center (side) excitonic bands to the Raman ω_R (IR ω_I) phonons of very different symmetries. This robust observation again supports the hidden threefold FSS structure. In addition, the 750 and 760 nm FT spectra do not scale each other, indicative of two different bright exciton states with slightly asymmetric coupling to the ω_I modes [9]. The multifold excitonic fine structure from these results shows that the middle dark states are brightened periodically by coherent phonons of Raman symmetry (black) and the bright ones are on two sides (blue and red). The narrow excitonic fine structure is consistent with the bright-dark splitting of ~ 3 nm shown in Fig. 2(a).

The time evolution of the *symmetry-selective* modes associated with bright and dark states deserves more attention. The quantum beat dynamics at 755 nm [Fig. 2(d)] at 4.2 K for the initial and for the extended 10 s of ps timescales (split axis) allow for the determination of the dephasing times of various vibronic modes. The Raman band, especially at the $\omega_{R1} \sim 0.8$ THz, is enhanced by coupling to the middle dark state in the 755 nm trace, Fig. 2(d), which is characterized by a long-lived, tens of ps vibronic coherence, for more than an order of magnitude longer than the bright ones in the 750 and 760 nm traces [Figs. 2(c) and 2(e)]. This is consistent with the optically forbidden dark states at the center. The exact dephasing

mechanism of the vibronic quantum beats is likely from a joint effect of the electronic correlation and Raman and IR phonon symmetry. Nevertheless, discovery of the quantum beats clearly reveal the *phonon symmetry-selective* coupling to the Rashba fine structure.

To put the observations on a strong footing, we have performed simulations based on an exciton Rashba FSS model, as proposed in Ref. [8]. The exciton FSS due to exchange interaction will be on the order of 0.1 meV for bulk crystal which is neglected in the simulation [2]. The further details are in supplementary. The Hamiltonian has the following form in the relative coordinate [9]

$$H = -\frac{\nabla_r^2}{2\mu} + V(r) + (\alpha_e \sigma_e - \alpha_h \sigma_h)\hat{n} \times i\nabla_r, \quad (1)$$

where $r = r_e - r_h$ with $r_e (r_h)$ for the electron (hole) (e and h) spatial coordinate. ∇ is the Laplace operator. The reduced mass μ is defined by $\mu^{-1} = m_e^{-1} + m_h^{-1}$. The Rashba term comes from a combined effect of spin-orbit interaction and inversion symmetry breaking (ISB), with ISB field in the $\hat{n}$ direction. Although the symmetry breaking source is still debated in perovskites, it can arise at the surfaces and/or bulk local internal structures. The optical spectrum of exciton Φ can be understood by the oscillator strength $f_\Phi \propto (|P_\Phi|^2/\omega_\Phi)$, with ω_Φ for exciton oscillator frequency and P_Φ for optical matrix element. The coupling between the exciton and phonon modes is investigated through phonon-modulated model parameters, including μ, α_e, α_h, and P_Φ. They exhibit sinusoidal modulations in time domain following the frozen phonon-induced atomic movement, as shown by DFT calculations (see the Supplemental Material [9]). Therefore, model simulations reported next use parameters in sinusoidal time modulations with amplitude from these DFT results.

The lowest energy solution of the above exciton Hamiltonian gives 1s exciton without Rashba interaction, which has fourfold degeneracy due to the electron doublet and hole doublet [8]. With the inclusion of nonzero Rashba term in MAPbI$_3$, the quartet ground state splits to a dark doublet, $|\Phi\rangle_{2,3}$, sandwiched between two bright states, $|\Phi\rangle_1$ and $|\Phi\rangle_4$ as marked in Fig. 1(b) (inset). Note, however, that the dark doublet is not entirely optically inactive because some amount of atomic orbital character mixing in the e and h states produce relatively small yet finite dipole matrix elements. The ratio is $1:0.1:2.2$ for the threefold FSS states from our calculations [9].

When different phonon modes in the system are excited by THz pump, the bright and dark exciton states respond in different manners. This is predicted by simulating snapshots of Rashba parameters and electronic transitions during one phonon cycle of a specifically tailored Raman (ω_{R1} mode $\sim$0.8 THz) and IR (ω_{I1} mode $\sim$2.0 THz) symmetries. This shows subcycle brightening of dark excitons by periodically modulating the Rashba parameters and

spin-split bands that are fully consistent with our observations. In Fig. 4, we plotted the coupling between the four lowest energy exciton states and the two most pronounced phonons identified, Raman ω_{R1} and IR ω_{I1} modes. By comparing the periodical control of the Rashba parameters under these two modes in Figs. 4(a) and 4(b), we clearly notice that the ω_{R1} has much bigger modulation to α_e and α_h. We attribute such distinct enhancement to the facts that the ω_{R1} mode introduces a much larger twist to the PbI$_6$ cage than the ω_{I1} mode and that the Pb-I frame directly determines the electronic band structure of MAPbI$_3$ near the Fermi level. As a result, it is clearly visible, that the ω_{R1} mode changes the band gap and oscillator strength of the dark states $|\Phi\rangle_{2,3}$ significantly, which gives rise to a pronounced ω_{R1} phonon modulation (blue circles), based on the model calculation in Fig. 4(c), i.e., subcycle coherent brightening of the dark excitons. In contrast, there is nearly no response to the ω_{I1} mode of the same amplitude (black circles). This is in excellent agreement with the experimental observations in Fig. 3. Moreover, we summarize the simulated results for the phonon amplitude dependence of the oscillator strength for the excitonic FSS states when coupled with ω_{I1} [Fig. 4(d)] and ω_{R1} [Fig. 4(e)] modes, respectively. For the ω_{I1} coupling in Fig. 4(d), the bright states $|\Phi\rangle_{1,4}$ (rectangle and triangle) exhibit bigger responses than the dark states $|\Phi\rangle_{2,3}$ (circles). The trend is clearly reversed for the ω_R coupling in Fig. 4(e). These simulations clearly explain the key mode-selective coupling data in Fig. 3.

Finally, we show that the experimentally observed $\Delta R/R$ spectral shape (red diamond) in Fig. 2(a) can be fitted well by two bright oscillators (blue line) centered at $\omega_{01} = 750.9$ and $\omega_{02} = 756.7$ nm, which correspond to the
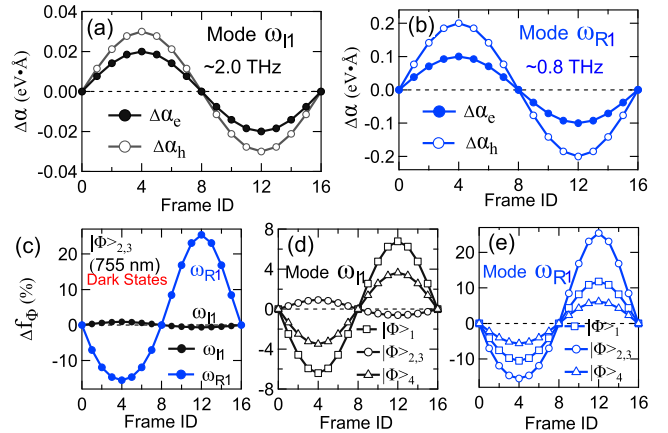

FIG. 4. Model calculation for the Rashba states induced by phonon modulation of IR and Raman symmetries. (a),(b) Changes of the Rashba parameters under ω_{I1} and ω_{R1} vibrations. (c) Oscillator strength changes calculated for the middle, two dark exciton states $|\Phi\rangle_{2,3}$ for 16 frames during one cycle of the lattice vibration. (d),(e) Mode-selective coupling to exciton FSS for ω_{R1} and ω_{I1} modes.

positive and negative peaks (dash lines). Specifically, the dielectric response can be modeled by [9]

$$\tilde{\varepsilon}(\omega) = 1 + \sum_{j=1,2} \frac{A_j}{\omega_{0j}^2 - \omega^2 + i\omega\tau_j^{-1}}. \qquad (2)$$

Pump-induced transient exciton generation affects $\Delta R/R$ signals by modifying $\tilde{\varepsilon}(\omega)$ via three main nonlinearities, i.e., bleaching (amplitude A_j decrease), broadening (scattering time τ_j decreases) and band gap renormalization (BGR) shifts in ω_{0j}. The best fit parameters can be found in the Supplemental Material [9]. Note that the small BGR shifts $\Delta\omega_{0j} = 0.1$ and 0.3 nm are within the spectral resolution, consistent with the stable spectra as a function of time seen in Fig. 2(a). In addition, the narrow, central dark states will not affect the transient spectra which are determined by the bright states. These results clearly show a Rashba splitting of the bright-dark states ~3 nm. This can only be resolved by the unique symmetry-selective, vibronic quantum beats and coherent dynamics shown in Figs. 2 and 3.

In conclusion, we use THz-driven quantum beat spectroscopy to unambiguously reveal the Rashba-type fine structure in MAPbI$_3$. This provides compelling implications for "Rashba engineering," i.e., periodic brightening of the dark excitons via modulation of Rashba parameters, for probing and controlling charge transfer and collection in photovoltaic devices. Our results also inspire merging quantum control [35], ultrafast phononics, and spintronics [36–39] to explore multifunction perovskite devices.

*jgwang@ameslab.gov
†These authors contributed equally to this work.

[1] S. D. Stranks and P. Plochocka, Nat. Mater. **17**, 381 (2018).
[2] M. A. Becker, R. Vaxenburg, G. Nedulcu, P. C. Sercel, A. Shabaev, M. J. Mehl, J. G. Michopoulos, S. G. Lambrakos, N. Bernstein, J. L. Lyons, T. Stöferle, R. F. Mahrt, M. V. Kovalenko, D. J. Norris, G. Rainò, and A. L. Efros, Nature (London) **553**, 189 (2018).
[3] Z. Liu et al., Phys. Rev. B **101**, 115125 (2020).
[4] F. Zheng, L. Z. Tan, S. Liu, and A. M. Rappe, Nano Lett. **15**, 7794 (2015).
[5] D. Giovanni, H. Ma, J. Chua, M. Grätzel, R. Ramesh, S. Mhaisalkar, N. Mathews, and T. C. Sum, Nano. Lett. **15**, 1553 (2015).
[6] P. Odenthal, W. Talmadge, N. Gundlach, R. Wang, C. Zhang, D. Sun, Z.-G. Yu, Z. V. Vardeny, and Y. S. Li, Nat. Phys. **13**, 894 (2017).
[7] K. Frohna, T. Deshpande, J. Harter, W. Peng, B. A. Barker, J. B. Neaton, S. G. Louie, O. M. Bakr, D. Hsieh, and M. Bernardi, Nat. Commun. **9**, 1829 (2018).
[8] M. Isarov, L. Z. Tan, M. I. Bodnarchuk, M. V. Kovalenko, A. M. Rappe, and E. Lifshitz, Nano Lett. **17**, 5020 (2017).
[9] See the Supplemental Material at http://link.aps.org/supplemental/10.1103/PhysRevLett.124.157401 for the detailed assignment of Raman and IR phonons and their motions and for further technical details of samples used and experimental setup and model, which includes Refs. [10–14].
[10] M. I. Saidaminov, A. L. Abdelhady, B. Murali, E. Alarousu, V. M. Burlakov, W. Peng, I. Dursun, L. Wang, Y. He, G. Maculan, A. Goriely, T. Wu, O. F. Mohammed, and O. M. Bakr, Nat. Commun. **6**, 7586 (2015).
[11] B. Adolph, J. Furthmüller, and F. Bechstedt, Phys. Rev. B **63**, 125108 (2001).
[12] G. Kresse and D. Joubert, Phys. Rev. B **59**, 1758 (1999).
[13] J. P. Perdew, K. Burke, and M. Ernzerhof, Phys. Rev. Lett. **77**, 3865 (1996).
[14] S. Grimme, J. Comput. Chem. **27**, 1787 (2006).
[15] Z. Liu, K. C. Bhamu, L. Liang, S. Shah, J.-M. Park, D. Cheng, M. Long, R. Biswas, F. Fungara, R. Shinar, J. Shinar, J. Vela, and J. Wang, MRS Commun. **8**, 961 (2018).
[16] A. N. Beecher, O. E. Semonin, J. M. Skelton, J. M. Frost, M. W. Terban, H. Zhai, A. Alatas, J. S. Owen, A. Walsh, and S. J. L. Billinge, ACS Energy Lett. **1**, 880 (2016).
[17] V. D'Innocenzo, G. Grancini, M. J. P. Alcocer, A. R. S. Kandada, S. D. Stranks, M. M. Lee, G. Lanzani, H. J. Snaith, and A. Petrozza, Nat. Commun. **5**, 3586 (2014).
[18] R. L. Milot, G. E. Eperon, H. J. Snaith, M. B. Johnston, and L. M. Hertz, Adv. Funct. Mater. **25**, 6218 (2015).
[19] T. J. Savenije, C. S. Ponseca, L. Kunneman, M. Abdellah, K. Zheng, Y. Tian, Q. Zhu, S. E. Canton, I. G. Scheblykin, T. Pullerits, A. Yartsev, and V. Sundström, J. Phys. Chem. Lett. **5**, 2189 (2014).
[20] M. Fu, P. Tamarat, H. Huang, J. Even, A. L. Rogach, and B. Lounis, Nano Lett. **17**, 2895 (2017).
[21] D. Niesner, M. Wilhelm, I. Levchuk, A. Osvet, S. Shrestha, M. Batentschuk, C. Brabec, and T. Fauster, Phys. Rev. Lett. **117**, 126401 (2016).
[22] D Cheng et al., J. Chem. Phys. **151**, 244706 (2019).
[23] M. Kozina, M. Fechner, P. Marsik, T. van Driel, J. M. Glownia, C. Bernhard, M. Radovic, D. Zhu, S. Bonetti, U. Staub, and M. C. Hoffmann, Nat. Phys. **15**, 387 (2019).
[24] K. Miyata, D. Meggiolaro, M. T. Trinh, P. P. Joshi, E. Mosconi, S. C. Jones, F. De Angelis, and X.-Y. Zhu, Sci. Adv. **3**, e1701217 (2017).
[25] T. Ghosh, S. Aharon, L. Etgar, and S. Ruhman, J. Am. Chem. Soc. **139**, 18262 (2017).

[26] F. Thouin, D. A. Valverde-Chávez, C. Quarti, D. Cortecchia, I. Bargigia, D. Beljonne, A. Petrozza, C. Silva, and A. R. S. Kandada, Nat. Mater. **18**, 349 (2019).

[27] H. Kim, J. Hunger, E. Cánovas, M. Karakus, Z. Mics, M. Grechko, D. Turchinovich, S. H. Parekh, and M. Bonn, Nat. Commun. **8**, 687 (2017).

[28] X. Yang, C. Vaswani, C. Sundahl, M. Mootz, P. Gagel, L. Luo, J. H. Kang, P. P. Orth, I. E. Perakis, C. B. Eom, and J. Wang, Nat. Mater. **17**, 586 (2018).

[29] X. Yang, C. Vaswani, C. Sundahl, M. Mootz, L. Luo, J. H. Kang, I. E. Perakis, C. B. Eom, and J. Wang, Nat. Photonics **13**, 707 (2019).

[30] L. Liang *et al.*, Nat. Commun. **10**, 607 (2019).

[31] X. Yang *et al.*, npj Quantum Mater. **5**, 13 (2020).

[32] C. Vaswani *et al.*, arXiv:1912.01676.

[33] A. M. A. Leguy, A. R. Goñi, J. M. Frost, J. Skelton, F. Brivio, X. Rodríguez-Martínez, O. J. Weber, A. Pallipurath, M. I. Alonso, M. Campoy-Quiles, M. T. Weller, J. Nelson, A. Walsh, and P. R. F. Barnes, Phys. Chem. Chem. Phys. **18**, 27051 (2016).

[34] L. Luo, L. Men, Z. Liu, Y. Mudryk, X. Zhao, Y. Yao, J. M. Park, R. Shinar, J. Shinar, K. M. Ho, I. E. Perakis, J. Vela, and J. Wang, Nat. Commun. **8**, 15565 (2017).

[35] C. Vaswani *et al.*, arXiv:1912.02121 [Phys. Rev. X (to be published)].

[36] T. Li, A. Patz, L. Mouchliadis, J. Yan, T. A. Lograsso, I. E. Perakis, and J. Wang, Nature (London) **496**, 69 (2013).

[37] X. Yang, L. Luo, M. Mootz, A. Patz, S. L. Bud'ko, P. C. Canfield, I. E. Perakis, and J. Wang, Phys. Rev. Lett. **121**, 267001 (2018).

[38] A. Patz, T. Li, X. Liu, J. K. Furdyna, I. E. Perakis, and J. Wang, Phys. Rev. B **91**, 155108 (2015).

[39] A. Patz, T. Li, L. Luo, X. Yang, S. Bud'ko, P. C. Canfield, I. E. Perakis, and J. Wang, Phys. Rev. B **95**, 165122 (2017).